Determination of the Quantum Dot Band Gap Dependence on Particle Size from Optical Absorbance and Transmission Electron Microscopy Measurements

Doris Segets,[†] J. Matthew Lucas,[‡] Robin N. Klupp Taylor,[†] Marcus Scheele,[§] Haimei Zheng,[§] A. Paul Alivisatos,[§] and Wolfgang Peukert[†,*]
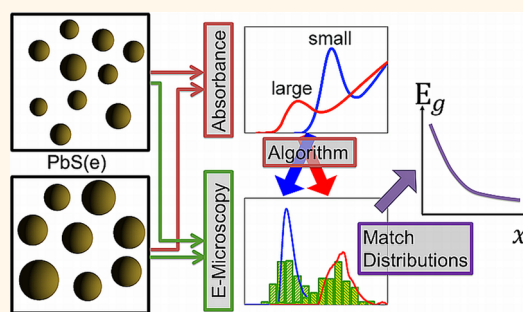
[†]Institute of Particle Technology, FAU Erlangen-Nuremberg, Cauerstr. 4, 91058 Erlangen, Germany, [‡]Department of Mechanical Engineering, University of California, Berkeley, California 94720, United States, and [§]Materials Science Division, Lawrence Berkeley National Laboratory, Berkeley, California 94720, United States

Semiconductor quantum dots (QDs) have found widespread interest during the past decade due to their tunable optoelectronic properties. Various material systems have been widely studied including those with absorbance features ranging from the UV (*e.g.*, ZnS or ZnO)[1] through the visible (*e.g.*, CdX, with X being S, Se, or Te)[2] up to the near-infrared (*e.g.*, PbS(e)).[3] For all of these workhorse systems, various synthetic routes and associated growth kinetics have been explored, and the resulting optical properties measured. As a result of this significant work, many of these materials are promising candidates for applications including solar cells,[4] field effect transistors,[5] or sensors.[6]

The fabrication of competitive QD-based devices is still challenging due to the manifold effects on the final performance. Restricting ourselves to colloidal QD suspensions, typical influencing factors include surface passivation, the chain length of the ligands,[7] and the level of doping,[8] in addition to the mean particle size[9] and, perhaps even more importantly, the particle size distribution (PSD). Besides the well-known quantum size effect which allows the absorption and emission spectral properties to be tuned, strong particle size dependency has also been reported in the behavior of QD field effect transistors and solar cells.[10] With respect to the PSD, Chandler *et al.*[11] stated that any dispersity in particle size leads to offsets in the energy levels and causes a net reduction in conductance of QD layers. On the other hand, Liu *et al.*[7] pointed out that as long as a percolating

network of large particles exists, charge transport is independent of particle size. Thus, a certain degree of polydispersity may be acceptable for certain applications. More recently, Zhitomirsky *et al.*[12] picked up this topic and investigated quantitatively the effect of larger sized PbS inclusions in a solar cell absorber layer comprising smaller sized PbS sample with narrow PSD.

ABSTRACT This work addresses the determination of arbitrarily shaped particle size distributions (PSDs) from PbS and PbSe quantum dot (QD) optical absorbance spectra in order to arrive at a relationship between band gap energy and particle size over a large size range. Using a modified algorithm which was previously developed for ZnO, we take only bulk absorption data from the literature and match the PSDs derived from QD absorbance spectra with those from transmission electron microscopical (TEM) image analysis in order to arrive at the functional dependence of the band gap on particle size. Additional samples sized solely from their absorbance spectra with our algorithm show excellent agreement with TEM results. We investigate the influence of parameters of the TEM image analysis such as threshold value on the final result. The band gap *versus* size relationship developed from analysis of just two samples lies well within the bounds of a number of published data sets. We believe that our methodology provides an attractive shortcut for the study of various novel quantum-confined direct band gap semiconductor systems as it permits the band gap energies of a broad size range of QDs to be probed with relatively few synthetic experiments and without quantum mechanical simulations.

KEYWORDS: quantum dot · optical properties · PbS(e) · automated TEM image analysis · absorbance spectra · particle size distribution

It was found that the recombination potential increases when the inclusion fraction exceeded 0.01%, whereas the open circuit voltage decreased at higher inclusion fractions of more than 1%.

The empirical developments described above clearly contribute to the understanding and industrial application of QD systems and are in part motivated by the lack of theoretical studies, particularly regarding the relationship between optical properties and particle morphology. If this relationship would be readily accessible, a clear characterization of the PSD influence throughout all process steps could be achieved. The starting point for this would be the large library of theoretical data which has been developed including descriptions of the size-dependent band gap energy $E_g(x)$ based on quantum mechanical approaches such as tight binding[13] or k·p models.[14] These models must be experimentally validated in order to show their relevance for real QD systems. This has been achieved through exhaustive studies for workhorse QD systems but less so for newer materials such as Cu_2ZnSnS_4 (CZTS).[15] Usually, validation requires the absorbance spectrum of a sample to be measured and the mean particle size to be evaluated from transmission electron microscope (TEM) micrographs. Then, this mean size is correlated with either the energy of the half-width maximum of the absorbance peak[16] or the absorption onset.[17] This approach, however, ignores the fact that most QD systems comprise a distribution of particle sizes, each size fraction contributing to the measured absorbance spectrum. Therefore, the deconvolution of the experimental absorbance spectrum into a suitably weighted sum of theoretical partial spectra would give access to a segment, rather than a single point on the band gap—particle size relationship. It would mean that, in principle, rather fewer experiments would need to be done in order to determine $E_g(x)$.

This approach was reported as early as 1994 by Mićić et al. for the case of InP QDs.[18] In that work, high-resolution (TEM) images were used to determine the PSD of a single sample. This was then used to construct a prediction of the sample absorbance spectrum using partial absorbance spectra which depended on an effective mass approximation (EMA)-like function for $E_g(x)$. Two exponents in the latter were used as free parameters to fit the absorbance spectrum prediction to the experimentally determined absorbance spectrum. The PSDs of further samples (assumed to have a log-normal form) could then be determined from their measured absorbance spectra using the now known function $E_g(x)$ to construct and summate partial absorbance spectra whose weighting coefficients were determined by fitting the mean size and standard deviation of the PSD. While the approach of Mićić et al.[18] showed promise for the determination of $E_g(x)$ and PSDs for realistic colloidal systems, the work has been largely forgotten in the literature. To the best of our knowledge, prior to our previous report,[19] the only significant works on absorbance to PSD conversion have been made by Pesika et al.[20] and Viswanatha and Sarma.[21] In the former case, a conversion based on the local slope of the absorbance band edge was used together with the EMA model, to determine an arbitrary PSD. Viswanatha and Sarma on the other hand followed the older approach, albeit assuming a normal distribution for the PSD and using a fixed relation $E_g(x)$ from literature rather than iteratively determining it from their own experimental data.[13] Their work also demonstrated that, in principle, such approaches are broadly applicable to a wide range of material systems. In our previous work, we showed that an arbitrary PSD can be extracted from absorbance spectra for ZnO QDs by an approach which deconvolutes appropriately weighted partial absorbance spectra from a measured spectrum, the corresponding size fractions being determined via the same tight binding model (TBM) for $E_g(x)$ that Viswanatha and Sarma used in their study.[13] With respect to the form of the partial absorbance spectra, we showed in agreement with the findings of Viswanatha and Sarma that its shape has little influence on the PSD determined from the absorbance measurement but strongly affects subsequent reconstructions of the absorbance spectra. The latter indicated the limitation of making this assumption. However, we demonstrated that the approach can be applied to quite arbitrary systems, such as those with a bimodal distribution, and subsequently used the approach successfully for the quantification of colloidal stability[22,23] and the determination of particle formation kinetics.[24] Nevertheless, a shortcoming of our approach when considered for the analysis of QDs of novel direct band gap materials is that tried and tested models or data sets for $E_g(x)$ do not exist.

In the present work, we demonstrate an approach to determine the size dependence of the fundamental band gap, $E_g(x)$, from only two QD samples whereby no assumptions are made regarding the shape of the PSD and no quantum mechanical model is necessary. In this work, PbS and PbSe were used due to the fact that their absorbance can be shifted over a wide wavelength range and that a wide range of models and data sets for $E_g(x)$ exist in the literature. Validation of our method with the latter indicated that the $E_g(x)$ curve determined via analysis of only two samples lies well within the spread of theoretical calculations and earlier experimental findings. We also show that the approach is insensitive to errors arising from TEM image analysis. Our method is expected to be applicable to various material systems and is highly relevant for rapid screening and optimization studies of current and next generation QD systems where TEM analysis may not be available or is otherwise prohibitive.
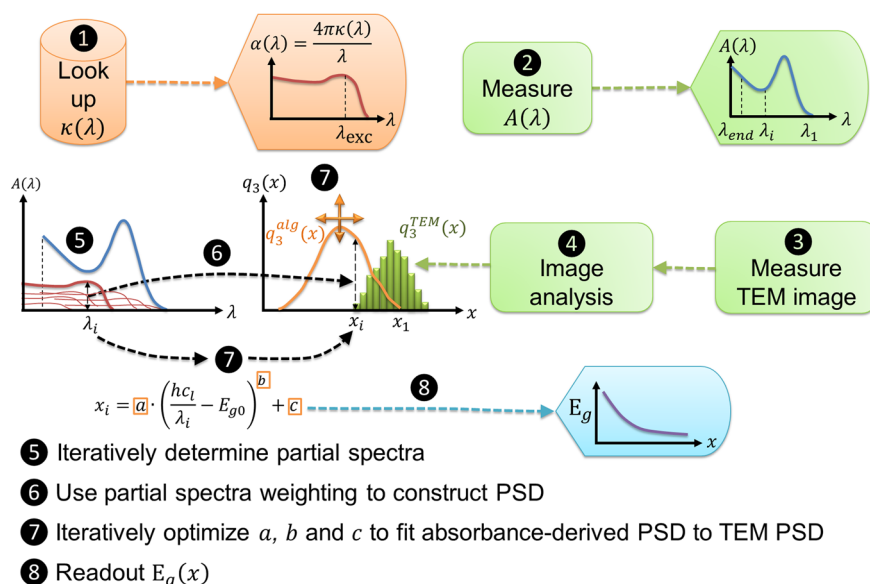
Figure 1. Schematic diagram showing our approach to converting a measured absorbance spectrum $A(\lambda)$ and corresponding TEM images for PbS(e) QDs into a relationship between band gap and particle size: $E_g(x)$.

RESULTS AND DISCUSSION

General Approach. The approach used in this work is based on the method we previously developed for ZnO[19] along with aspects from Mićić et al.[18] The prerequisites are that the particles to be analyzed comprise a direct band gap semiconductor material and are small enough to manifest quantum confinement effects. Furthermore, the particles should exhibit negligible light scattering in the wavelength range of interest; that is, they are Rayleigh scatterers. In the present work on PbS(e), we take as input the measured absorbance spectrum and TEM images of the corresponding sample. Furthermore, since the only literature data used are the imaginary part of the refractive index, $k(\lambda)$, determined by spectroscopic ellipsometry,[25,26] the target function $E_g(x)$ must be adjusted until the TEM-derived PSD, $q_3^{TEM}(x)$ is matched by that determined by our algorithm $q_3^{alg}(x)$.

Our general approach is illustrated in Figure 1. At the heart is an algorithm which deconvolutes the measured absorbance spectrum $A(\lambda)$ into partial spectra $A_i(\lambda)$. Each of these is taken to have the form of the bulk absorption spectrum

$$\alpha(\lambda) = 4\pi\kappa(\lambda)/\lambda \tag{1}$$

of the material in question, an assumption which has already been discussed and justified by Mićić et al.,[18] Viswanatha and Sarma,[21] and us.[19] Recently, Hens and Moreels indicated that for some QD systems work toward determining more realistic partial spectra is indeed quite mature;[27] however, a detailed comment on the use of the bulk absorption data is found in the Supporting Information S1.

To reconstruct the absorbance spectrum, we arrange eq 1 such that the exciton peak position of each partial spectrum is shifted so as to correspond to one of the wavelengths in the original spectrum

$$A_i(\lambda) = f_i\alpha(\lambda - \lambda_i + \lambda_{exc})d_c \tag{2}$$

where λ_{exc} is the exciton peak position in the bulk absorption spectrum, d_c is the measurement cell path length and

$$\lambda_i = hc_l/(\Delta E_i + E_{g0}) \tag{3}$$

in which ΔE_i is the energy difference between a particle band gap energy $E_{gi} = hc_l/\lambda_i$ and the bulk band gap E_{g0} (with c_l being the speed of light and h being Planck's constant). The bulk band gaps of PbS and PbSe were taken to be 0.41 and 0.28 eV, respectively.[28] The magnitude of each partial spectrum is adjusted via parameter f_i so that the spectrum's contribution to the overall absorbance spectrum can be determined. This is achieved by iteratively subtracting partial spectra from the measured spectrum for successively decreasing λ_i (i.e., $\lambda_{i+1} < \lambda_i$). Hence, the weighting $g_3(x_i)$ of the corresponding particle size fraction

$$x_i = a\left(\frac{\Delta E_i}{eV}\right)^b + c \tag{4}$$

can be determined according to

$$g_3(x_i) = \frac{f_i}{\Delta x_i} = \frac{A(\lambda_i) - \sum\limits_{1}^{i-1} f_j\alpha(\lambda_i - \lambda_j + \lambda_{exc})d_c}{\alpha(\lambda_{exc})\Delta x_i d_c} \tag{5}$$

where $\Delta x_i = \Delta x_{i+1} - x_i$.

To ease a future implementation for other direct band gap QDs, the MATLAB code used for PbS(e) is exemplarily provided together with one set of measurement data in the Supporting Information. It should be noted that eq 5 has been incorporated into these
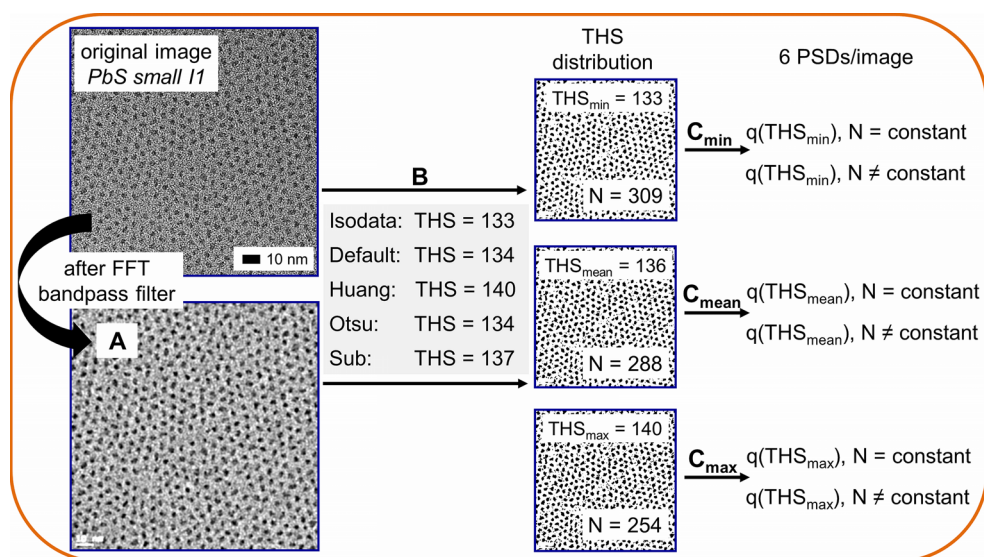
Figure 2. General approach regarding the treatment of TEM micrographs exemplarily shown by means of the smaller size fraction of PbS starting from the original image which is processed by a band-pass filter (step A) and analyzed in terms of a threshold (THS) distribution (THS$_{min}$, THS$_{mean}$, and THS$_{max}$) in the subsequent step B; to ensure that the same particles are compared, the position of the particles is discriminated in the last step C by the center of gravity; accordingly, from one TEM micrograph, six PSDs are obtained to prove that the TEM evaluation has no effect on the final results.

codes in such a way that any negative values which arise when subtracting the partial spectra from the measured spectrum are set to zero. Within these code examples, we provide the option to use—instead of the bulk absorption data sets as indicated in Figure S4_1—step functions that lead to almost the same results. It should also be noted that this would be the appropriate position for a future implementation of size-dependent extinction data. Within eqs 2 and 5, a size-dependent extinction coefficient could be introduced by a size-dependent prefactor incorporated in parameter f_i.

Regarding our approach, initial guesses of the coefficients a [nm], b [−], and c [nm] are then made, leading to the construction of the volume weighted size distribution $q_3^{alg}(x_i) = C \times g_3(x_i)$, where C is a constant which ensures the total area under the distribution is unity. Coefficients a, b, and c are adjusted to generate a best match between the derived distribution ($q_3^{alg}(x_i)$) with that determined by TEM image analysis ($q_3^{TEM}(x)$). Finally, the expression $E_g(x) = E_{g0} + ((x − c)/a)^{1/b}$ can be used to plot the size dependence of the band gap of the material. As we shall discuss later in the context of the measured materials, it is preferable to analyze two samples covering two different particle size regimes in order to arrive at compromise values for a, b, and c resulting in a function for $E_g(x)$ which is valid over a wide size range. This underlines once more the rationality of our approach as only the TEM image analysis of as few as two samples enables the PSD of any future sample to be determined *via* a rapid and low-cost absorbance measurement.

Image Analysis. The above description of our approach shows that TEM image analysis is a critical factor influencing the function $E_g(x)$. We therefore considered how image analysis might introduce errors into the PSD ($q_3^{TEM}(x)$) and how these errors manifest themselves in $E_g(x)$. Due to the extremely small size of QDs and the interference of the amorphous carbon substrate, accurate PSD determination from TEM images is virtually impossible without introducing a certain degree of subjectivity. In the case of Mićić *et al.*, for instance, particle size was related to the number of observable lattice fringes in each particle in the image.[18] This might be problematic since QDs generally do not have an aspect ratio of unity and since phase contrast at particle edges may be different from that in the bulk. In our case, the entire image analysis is performed using the freely available software ImageJ.[29] We carry out an automated analysis of a black-and-white binary image which determines the area of separated regions of black pixels (the particles) against a white background.

Two major sources of error must be eliminated in order to achieve a realistic size distribution from TEM images. First, the thresholding process which produces the binary image from the original grayscale image should clearly identify the particle boundaries; that is, it should not erode or dilate the particles. Second, the analysis process should distinguish between isolated and aggregated particles. While the second issue is easily resolved, the former is not. Therefore, we explored different thresholding regimes in order to arrive at an understanding of the influence of this process on $q_3^{TEM}(x)$ and ultimately $E_g(x)$.

Figure 2 illustrates our systematic approach to handling and analyzing TEM images for the case of a sample of small PbS particles. Further micrographs of this sample, equivalent treatment for large PbS particles, and both small and large PbSe particles are

found in the Supporting Information (see Figures S2_1−S2_4).

It is evident that, due to the amorphous carbon background, a clear distinction of the particle edges from the original micrograph is difficult to achieve. Therefore, a FFT band-pass filter was applied (process A in Figure 2) to remove high and low spatial frequencies. The lower limit of filtering was set to a feature length of 1 nm to distinguish the particles from the substrate, and the upper limit was set to a feature length of 25 nm as this is the maximum spacing between two particles. The resulting image clearly allows better resolution of the particles. The next step, the threshold adjustment (process B in Figure 2), is the most crucial part of the image analysis process. In this operation, the 8-bit gray-scale image is converted to a binary image by defining a certain grayscale cutoff value which is denoted as the threshold (THS) value. Accordingly, all tones at or below the THS value become white, whereas all tones above the THS value become black. In addition to manual thresholding, ImageJ provides a set of 16 built-in automated thresholding routines. A simple screening of these using typical FFT-filtered TEM images determined that most could be discounted as they failed to identify the particle edges (see examples in the Supporting Information S3). The four remaining thresholding routines that seemed appropriate to our TEM micrographs were *Isodata* and *Default*,[30] *Huang*,[31] and *Otsu*.[32] In addition, for every image, we carried out manual subjective thresholding (THS$_{sub}$). In this case, THS was varied until the operator (DS) was satisfied that the edges of the particles were best covered. Figure 2 shows the five values of THS obtained for the micrograph in question. In order to gain an understanding of the spread of PSDs obtained through image analysis, we identified from these a minimum (THS$_{min}$), mean (THS$_{mean}$), and maximum (THS$_{max}$) THS value (Figure 2). Interestingly, THS$_{min}$ and THS$_{max}$ were always obtained using the *Isodata* and *Huang* routines, respectively.

The final process in the image analysis is the identification and measurement of particles from the thresholded binary image, a procedure which is fully automated in ImageJ and allows for the designation of a search range in terms of particle sizes and spheri-cities. From the projection area provided by ImageJ, the particle size of small and large PbS(e) was calcu-lated by assuming a circle ($x = (4A/\pi)^{1/2}$). In case of PbS, we permitted the inclusion of particles with sphere equivalent diameters between 2.2 and 7 nm and with sphericity values greater than 0.7. For the PbSe micro-graphs, sizes up to 15 nm were used, and lower sphericity values down to 0.3 were applied. Due to the better contrast achieved for the larger sized PbSe QDs, the particles were easily distinguished from the carbon grid. Thus, a strict sphericity criterion was not needed to separate particles from "noise".

At this point, it should be mentioned that this kind of particle evaluation is only applicable for the QD particle sizes used around the magnifications shown in this study. At lower magnifications, an error as small as one pixel had a comparatively large impact on the final result. In contrast, for much higher magnifications, the fuzziness at the particle edges arising from the interference from the amorphous carbon background was too large. In general, on the basis of the experience developed in the present study, we consider a max-imum deviation of the PSDs well below 0.5 nm throughout the threshold distribution to be accept-able. However, as requirements might change from one case to another, further studies are needed to give a clearer advice on the allowed error.

A further observation was that, for increasing THS, the number of detectable particles decreased (see Figure 2). This was due to the bridging or stretching of particles which led to their elimination *via* the sphericity criterion. In order to eliminate the possibility that this effect considerably skewed the resulting PSD, we determined size distributions for each THS value for two cases (process C in Figure 2). In the first, only the particles which appeared in all three images were analyzed (N = constant). This was achieved in a semi-automated fashion by looking for matches in the center area of particles in the resulting data sets. In the second case, all detectable particles in each image were analyzed ($N \neq$ constant). Thus, for each image, a total of six different number weighted PSDs were produced. Each PSD was generated by determining the volume equiva-lent sphere diameter for each particle, counting the number of particles N_k in each size interval of $\Delta x_k = 0.2$ nm over the whole size range and expressing as

$$q_0^{TEM}(x_k) = \frac{N_k}{\Delta x_k \sum N_k} \tag{6}$$

In order to compare directly with $q_3^{alg}(x)$ distribu-tions determined from absorbance measurements, $q_0^{TEM}(x_k)$ values were converted into volume weighted PSDs by the standard formula using the third moment of the number density distribution $M_{3,0}$:[33]

$$q_3^{TEM}(x_k) = \frac{x_k^3 \cdot q_0^{TEM}(x_k)}{\underbrace{\sum(x_k^3 \cdot q_0^{TEM}(x_k) \cdot \Delta x_k)}_{M_{3,0}}} \tag{7}$$

Figure 3a,c summarizes the PSDs obtained from TEM micrographs according to the procedure de-scribed above for samples of large and small QDs of PbS and PbSe, respectively. Comparing in Figure 3a the PSDs of PbS derived for N = constant and $N \neq$ constant, the number of evaluated particles has a negligible influence on the final PSD. This is ascribed to the fact that even for the case of N = constant more than 100 particles were evaluated and that only "correct" parti-cles are able to meet the size and sphericity criteria
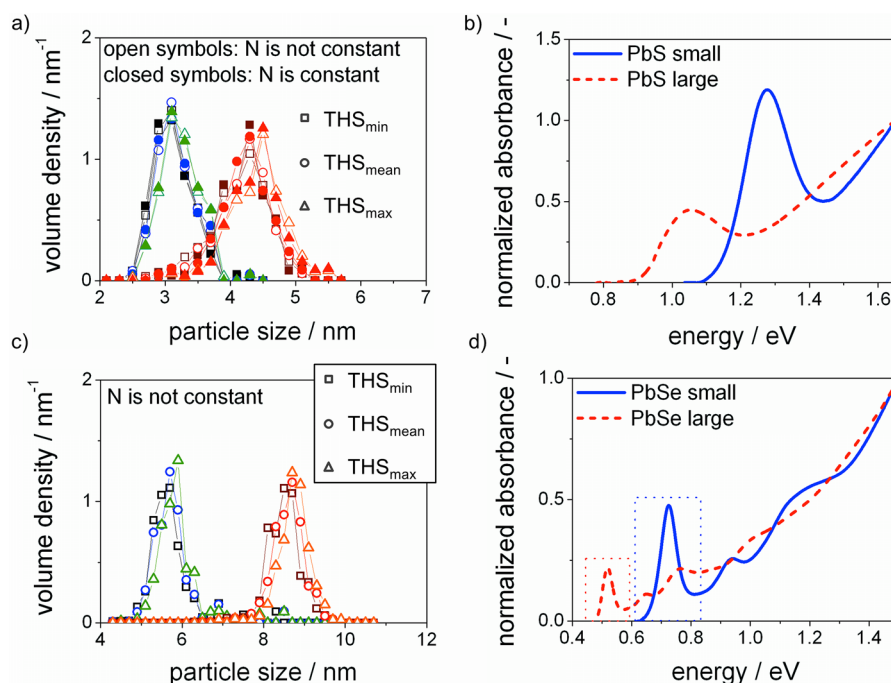
Figure 3. (a) PSDs derived from TEM micrographs for small and large PbS QD samples throughout the THS distribution (THS$_{min}$, squares; THS$_{mean}$, circles; and THS$_{max}$, triangles) after having all particles evaluated (open symbols) as well as after having discriminated the position of the particles to ensure that only particles appearing for every THS value are compared (closed symbols). (b) PbS absorbance spectra on an energy scale measured for the small (blue solid line) and the large (red dashed line) particle sample. (c,d) Experimental results for PbSe with respect to PSD and absorbance; the color and symbol code are the same as shown for PbS; the absorbance spectra of PbSe also show higher order excitonic transitions; however, the energy range considered for the derivation of PSD is highlighted by dotted frames. The absolute number of particles evaluated for every size histogram (at least 105) is summarized in Table 1.

TABLE 1. Mean Volume Weighted Particle Sizes $x_{1,3}$ of PbS and PbSe Derived for Different THS Values[a]

	$N \neq$ constant			$N =$ constant		
	$x_{1,3}$(THS$_{min}$)/nm	$x_{1,3}$(THS$_{mean}$)/nm	$x_{1,3}$(THS$_{max}$)/nm	$x_{1,3}$(THS$_{min}$)/nm	$x_{1,3}$(THS$_{mean}$)/nm	$x_{1,3}$(THS$_{max}$)/nm
PbS small	3.1	3.2	3.2	3.1	3.2	3.2
PbS large	4.1	4.2	4.4	4.2	4.2	4.4
PbSe small	5.7	5.7	5.9	—	—	—
PbSe large	8.5	8.6	8.7	—	—	—
	N(THS$_{min}$)/—	N(THS$_{mean}$)/—	N(THS$_{max}$)/—	N(THS$_{min}$)/—	N(THS$_{mean}$)/-	N(THS$_{max}$)/—
PbS small	309	288	254	242	242	242
PbS large	171	167	124	105	105	105
PbSe small	172	176	168	—	—	—
PbSe large	226	237	258	—	—	—

[a] For PbS, also the results for different THS values and under consideration of varying or identical particles, respectively, are shown ($N =$ constant); finally, the absolute numbers of evaluated particles are summarized.

described above. Accordingly, for a constant threshold, the distributions for $N =$ constant and $N \neq$ constant are nearly identical (compare open and closed symbols in Figure 3a). Thus, for PbSe, the discrimination of particles according to their center of area as described for PbS above was not performed.

Compared now to the PSDs of both PbS and PbSe for different THS values, a small but noticeable influence of the threshold is identified. This manifests itself as a slight shift to larger particle sizes as the threshold

increases and is also reflected by the mean volume weighted particle sizes ($x_{1,3} = \sum(x_k q_3^{TEM}(x_k)\Delta x_k)$) which are summarized in Table 1. Here, a shift of 0.1 to 0.3 nm is seen when one goes from THS$_{min}$ to THS$_{max}$. Although this appears to be small and most likely acceptable for the fitting procedure, all three data sets (denoted as THS$_{min}$, THS$_{mean}$, and THS$_{max}$) will be used in the next section to establish any influence of the different thresholds on the determined particle size versus band gap relationship $E_g(x)$.
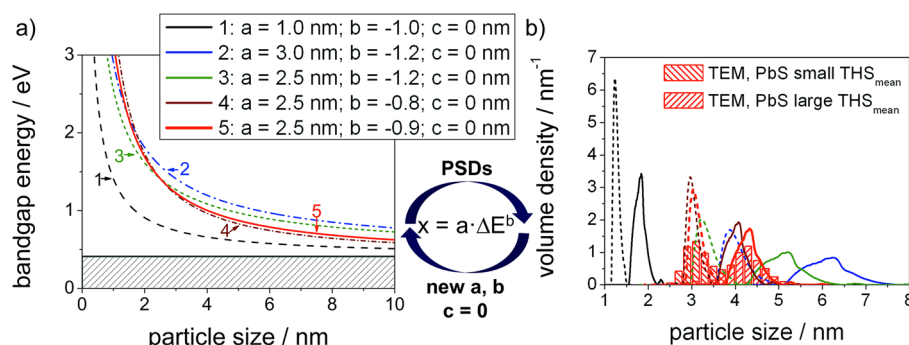
Figure 4. (a) Evolution of PbS band gap *vs* particle size derived by matching $q_3^{alg}(x)$ with $q_3^{TEM}(x)$ exemplarily shown for five different *a,b* pairs (*c* = 0 nm). (b) Corresponding PSDs $q_3^{alg}(x)$ for the small (dashed lines) and the large (solid lines) particle size samples together with the TEM distributions $q_3^{TEM}(x)$ (red bars) derived by using THS$_{mean}$. The number of evaluated particles (*N* = 105 and *N* = 242, respectively) can also be extracted from Table 1.

Derivation of Particle Size *vs* Band Gap Relationship. Having presented our approach for the derivation of PSDs from absorbance spectra (Figure 1) and from TEM images (Figure 2), we now demonstrate how combining these can lead to the generation of a realistic expression for $E_g(x)$. The absorbance spectra used for the determination of $q_3^{alg}(x_i)$ are shown in Figure 3b,d for PbS and PbSe, respectively. Once more, we emphasize that the deconvolution into partial spectra is only based on the first excitonic transition. Hence, for PbSe, the corresponding data intervals used for the analysis of the absorbance measurements are highlighted by red and blue boxes in Figure 3d. The bulk absorption spectra $\alpha(\lambda)$, which define the form of the partial spectra used to reconstruct the measured absorbance spectra, are shown in the Supporting Information (see Figure S4_1).

Figure 4 demonstrates our approach for determining $E_g(x)$ for the case of PbS. For the matching of the PbS data, eq 4 could be simplified by setting *c* to 0 nm and only the parameters *a* and *b* were adjusted to generate an acceptable match. In contrast, for PbSe, the increase of $E_g(x)$ is less steep and thus all three parameters had to be considered, as otherwise, a match of both the small and the large particle size fraction for one set of parameters is not possible. However, apart from this, the methodology used in the case of PbSe was identical to PbS and can be seen in the Supporting Information (see Figure S5_1). As we discussed in relation to Figure 1, PSDs determined from the measured absorbance spectra *via* our algorithm for large and small QDs were compared with the corresponding TEM-derived PSDs. Figure 4a shows the resulting plot of $E_g(x)$ and Figure 4b the corresponding size distributions for a number of different *a,b* pairs along with the PSDs from TEM image analysis. For the case of *a* = 1 nm and *b* = −1 (curve 1), it is evident that the positions of the PSDs for the two samples derived from the absorbance spectra are grossly underestimated. Curves 2 and 3 are also a rather poor fit, being overestimated for both samples. Curve 4 is a reasonable fit to the smaller size fraction but not for the larger.
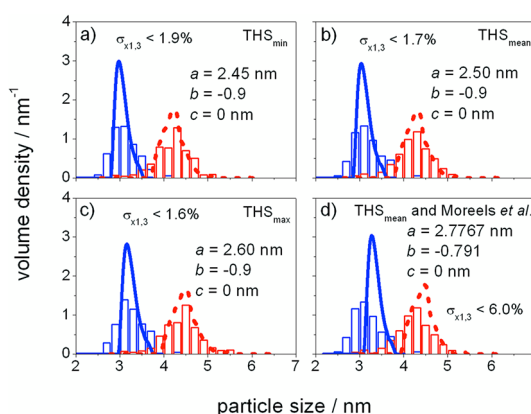

Figure 5. Results of PSD^{alg} (blue solid and red dashed line) showing the best match with the PSD^{TEM} (blue and red bars) presented together with the results for the parameters *a*, *b*, and *c* and the relative deviations of the mean particle size $\sigma_{x1,3}$ using (a) THS$_{min}$, (b) THS$_{mean}$, and (c) THS$_{max}$. (d) Additionally, the PSD^{alg} values obtained by using the literature correlation of Moreels *et al*.[36] (blue solid and red dashed line) are compared to the PSD^{TEM} values obtained by using THS$_{mean}$; to derive a function for $\Delta E_i(x)$ from the data of Moreels *et al*.,[36] we plotted the literature curve in the form of $x_i = f(\Delta E_i)$ and fitted it with $x_i = a(\Delta E_i/eV)^b$ (R^2 = 0.9981). The number of evaluated particles (at least 105) can be extracted from Table 1.

A compromise is arrived at for curve 5 (*a* = 2.5 nm, *b* = −0.9) where the position of each size fraction is reasonably matched. Nevertheless, some discrepancy is seen for the very smallest sizes for the sample of small particles. Whether this arises from our algorithm or the TEM evaluation (or both) cannot be confirmed without an additional independent measuring technique, such as analytical ultracentrifugation (AUC).[34,35] However, the general agreement between the PSDs is already very good, and also, the slight tailing of the sample with larger size is reflected by the result from the absorbance spectrum conversion algorithm.

We now consider how $E_g(x)$ determined by our approach might be influenced by the THS value used during image analysis. Figure 5 shows the matching of the PSDs derived from absorbance spectra with those from TEM image analysis for the case of threshold values
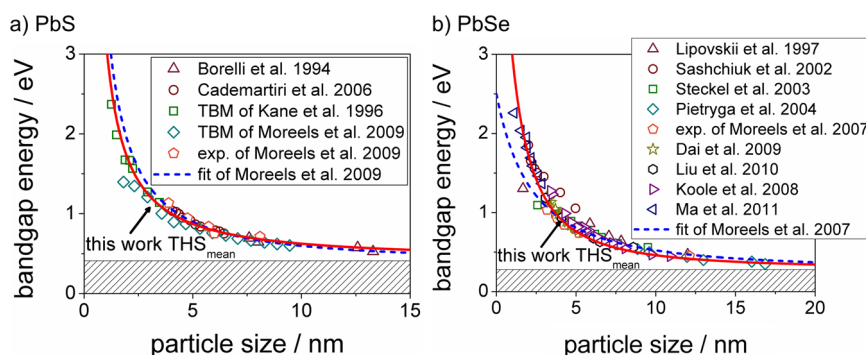
Figure 6. Relationship between the fundamental band gap energy and particle size as derived in our work along with comparison to literature data for (a) PbS[36−39] and (b) PbSe[7,10,40−46] as indicated.

THS$_{min}$ (Figure 5a), THS$_{mean}$ (Figure 5b), and THS$_{max}$ (Figure 5c). The corresponding a, b, and c values used to achieve the matching shown are indicated. The equivalent data for PbSe are provided in the Supporting Information (see Figure S6_1 and Table S6_1). It is clear that while b remains constant, the value of a has to increase slightly to account for the marginal shift of the PSDs to larger sizes with increasing THS value ($c = 0$ nm). The good match of the PbS(e) data is also reflected by the deviations in $x_{1,3}^{alg}$ in comparison to $x_{1,3}^{TEM}$ denoted as $\sigma_{x1,3}$ ranging from 1.6% (2.0%) in the case of THS$_{max}$ (THS$_{mean}$) to a maximum value of 1.9% (2.9%) in the case of THS$_{min}$ (THS$_{min}$, for details about PbSe, see Supporting Information S6).

To put these differences into perspective, we also extracted the PSD from absorbance spectra using, instead of eq 4, the functional relationship between band gap and size for PbS QDs which was determined by Moreels et al.:[36]

$$\Delta E_i = \frac{1 eV}{0.0252\left(\dfrac{x}{nm}\right)^2 + 0.283\left(\dfrac{x}{nm}\right)} \tag{8}$$

The resulting absorbance-spectra-derived PSDs are compared with those from TEM image analysis (using THS$_{mean}$ for the THS value) as shown in Figure 5d. It is evident that while a reasonable match of the larger sized sample is obtained, this is not the case for the smaller QDs. For the case of PbSe, the discrepancy is even more pronounced due to the low slope of $E_g(x)$ below 0.6 eV (see Figure S6_1 and Figure S7_1). Thus a small energy difference ΔE_i can have a comparatively large impact on the correlated particle size.

The discrepancy with the $E_g(x)$ relationship from the literature discussed above raises the question whether this mismatch is a result of systematic errors in the actual TEM analysis (e.g., instrumental error) or whether it is due to a certain mismatch with the $E_g(x)$ function of Moreels et al.[36] To establish this, we superimposed our $E_g(x)$ function corresponding to the best matching of PSDs (i.e., curve 5 in Figures 4a and S5_1a) with datasets from various studies of colloidal PbS(e) QDs (Figure 6). We obtained the latter for PbS from the excellent data

set in the work of Moreels et al.[36] which, in addition to their own experimental and theoretical data points, summarizes experimental work of Cademartiri et al.[37] as well as Borelli and Smith[38] together with the results of TB calculations according to Kane et al.[39] For PbSe, Moreels et al.[40] also carried out a similar study some years before in which they again provided a good $E_g(x)$ curve together with their own experimental data points and data from the literature.

Accordingly, Figure 6a,b shows the comparison of our derived $E_g(x)$ with previous studies of PbS and PbSe, respectively. The values for parameters a, b, and c are summarized in the Supporting Information (see Table S6_1). It can be immediately inferred that our $E_g(x)$ curves lie well within the bounds of most literature data and crucially appear to correspond well to data points obtained at both smaller and larger sizes. We therefore highlight this result as justification for the matching of PSDs of two samples rather than one, as was demonstrated in Figure 4. Indeed, our work indicates that the functional form of $E_g(x)$ can be determined for a wide portion of the quantum size regime when absorbance and TEM data are acquired from just two samples and where no form of PSD (lognormal etc.) must be specified. However, it should be pointed out that our approach is not intended as an improvement of or substitution for sophisticated quantum mechanical calculations. We consider it as an alternative for the rapid characterization of colloidal QDs, especially those of novel composition and the derivation of the size dependence of their band gap as directly tuned to the needs of a certain experiment or application. Moreover, for a successful larger-scale production of QDs, access to the whole PSD throughout all unit operations is seen as a key step for process control.

Further Verification of the Approach. To verify our algorithm, an unknown sample of even larger PbS QDs with a modal size of around 6 nm was synthesized. The corresponding absorbance spectrum (Figure 7a) was converted to PSDs using the $E_g(x)$ curves (see Figure 6a and Figure S7_1a) determined above for THS$_{min}$, THS$_{mean}$, and THS$_{max}$ (Figure 7b−d). A very good
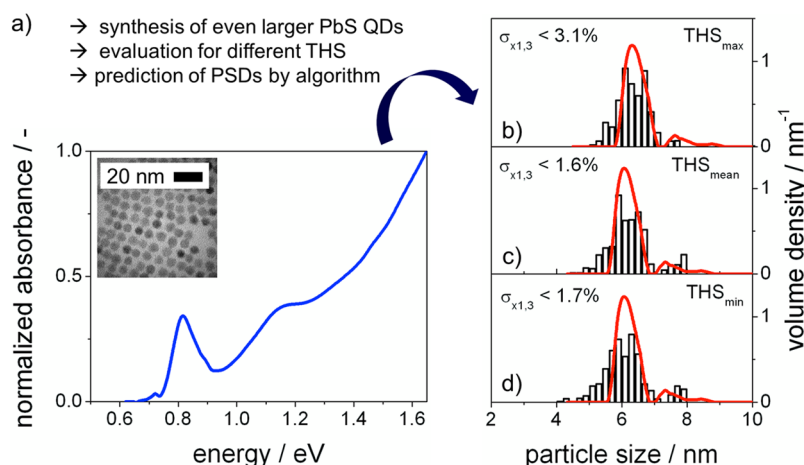
Figure 7. (a) Absorbance measurement and typical TEM micrograph of the third PbS sample with unknown PSD. (b−d) Comparison of the PSD results obtained from TEM image analysis using (b) THS_{max} ($N = 131$), (c) THS_{mean} ($N = 190$), and (d) THS_{min} ($N = 230$) (bars) with the PSDs calculated by the algorithm using parameters a, b, and c as they are indicated in Table S6_1.
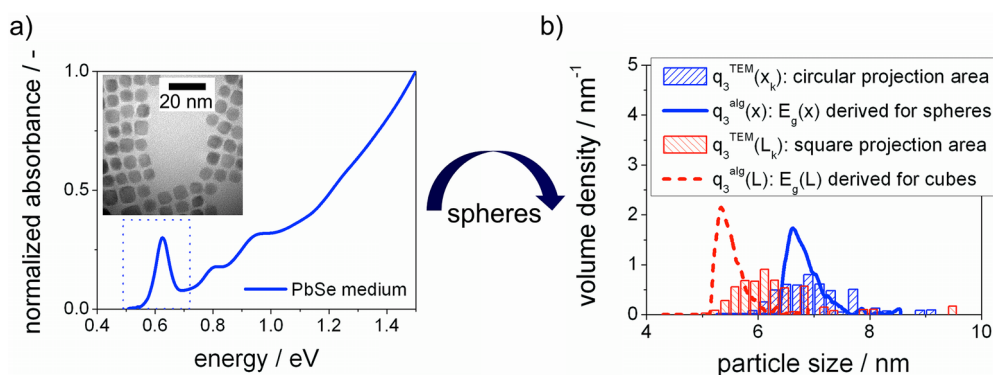

Figure 8. (a) Typical TEM micrograph and normalized absorbance spectrum of the medium sized PbSe nanoparticles (the first excitonic peak used for evaluation is highlighted by a blue dotted frame). (b) Comparison of PSD^{TEM} for medium sized PbSe particles derived for THS_{mean} ($N = 123$) and the assumption of a cubic (red) or a spherical (blue) particle shape together with the calculated PSD^{alg} (with parameters a, b, and c matched with THS_{mean} and (with)out eq 9).

agreement between the results of the PSD^{alg} and the measured PSD^{TEM} was obtained with deviations in $\sigma_{x1,3}$ ranging from 3.1% in the case of THS_{max} down to even below 1.6% when the analysis was performed for THS_{mean} (Figure 7c). Additionally, we prepared a smaller sized sample of PbSe QDs with a modal size of around 2.6 nm (Figure S8_1). Though the TEM evaluation was challenging as discussed in more detail in Supporting Information S8, the PSD^{alg} matches the expectations from TEM with respect to the size range of the PSD. These results confirm once more the wide applicability of our band gap versus size relationships—even though they were derived from rather differently sized samples (for PbS, PSDs situated around ∼3.1 and ∼4.3 nm; for PbSe, PSDs situated around ∼5.8 and ∼8.6 nm). Accordingly, we would give for PbS a validated size range from 3 to 7 nm and in case of PbSe a validated range from 2.5 to 10 nm.

Prior to concluding this work, we wish to comment on the application of our approach to nonspherical particles. In addition to the large and small particle samples, a third sample of PbSe was produced with an intermediate mean size of around 7.1 nm (Figure 8). Compared to the samples discussed earlier, this one showed a borderline tendency toward cubic particle formation (see Figure 8a, inset). This behavior is well-documented in literature and a result of energy differences in between the [100] and [111] facets once the crystal has reached a critical size.[47−49] Above this size, the spherical shape which has the smallest surface-to-volume ratio of all geometric forms transforms into either a cube or an octahedron by eliminating the facets of higher energy. The exact reaction pathway depends on the surfactant and its purity.

In any case, it is clear that the particle shape assumed for the evaluation of the projection area derived by TEM image analysis will strongly influence $q_3^{TEM}(x)$. We therefore used the $E_{g,PbSe}(x)$ relationship determined from the small and the large sized samples to establish if the medium sized particles can be still treated like spheres or if they are better described by cubes.

In case of PbSe cubes, Allan and Delerue reported that $E_{g,PbSe}(x)$ can be easily translated when the diameter

of a sphere is converted into a side length of a volume-equivalent cube by[50]

$$L = x(\pi/6)^{1/3} \tag{9}$$

For the image analysis, we assumed, respectively, circular and square cross sections (or projection areas) for all three threshold conditions described above. The equivalent size was determined by applying a constant shape factor $k_A = (4/\pi)^{1/2}$. In the following, only the results for THS_{mean} are discussed; the data derived for the other THS values are shown in the Supporting Information (see Figures S9_1 and S9_2).

Figure 8b shows the comparison of the corresponding TEM-measured PSDs derived for circular or square projections with those determined from the absorbance spectrum (Figure 8a). Regarding the algorithm, eq 4 was either used directly (i.e., by matching the TEM distribution THS_{mean} with that from the algorithm using the previously determined parameters a, b, and c) or translated for cubic-shaped particles by multiplication with $(\pi/6)^{1/3}$ according to eq 9. It is clear that the TEM evaluation assuming spherical particles provides an excellent match with the calculated PSD^{alg} with a maximum deviation in the mean volume weighted particle size $\sigma_{x1,3}$ below 3.7% when using THS_{min} (for THS_{mean} and THS_{max}, the deviation is even smaller than 3.5 and 2.7%, respectively), whereas the evaluation assuming cubic particles clearly underestimates the particle size. Thus, though the particles on the TEM grid appear cube-like at first glance, they are still properly described by spheres regarding the quantum confinement of their first excitonic transition.

CONCLUSION

In summary, the present work has described a method to experimentally determine the relationship between the fundamental band gap energy for direct band gap semiconductor quantum dots and their size, using a small number of measurements on samples with arbitrary particle size distribution (PSD). PbS and PbSe were chosen as well-described model systems whose size induced band gap shifts lead to large shifts of their absorbance spectra. For the derivation of the band gap versus size relationship, a previously developed algorithm which enables the calculation of arbitrary PSDs from optical absorbance spectra was modified. In contrast to our previous work on ZnO, we used literature data on the bulk absorption properties only and employed matching of the derived PSDs with those from TEM image analysis in order to arrive at a suitable function for the band gap versus size relationship. We explored the influence of aspects of the TEM image analysis such as threshold value on the final result and concluded that the method is fairly insensitive to variabilities in the handling of images.

In general, we found good correspondence between the band gap versus particle size relationship determined in this work and literature data. Our work showed that by considering not only a mean particle size but rather the overall PSD it is possible to derive the evolution of the fundamental band gap with particle size over a wide size range by using only two differently sized samples. Moreover, due to its high sensitivity toward small changes in the band gap versus size relationship, it might become a starting point for the systematic characterization of nonspherical particle shapes, too.

Finally, the present approach is not related to any quantum mechanics calculations as it is only based on experimental data. This will not replace the need for sophisticated theoretical calculations but is another technique that gives access to the band gap energy of quantum dots and is expected to become relevant for the rapid evaluation of novel, less well-described material systems in the future.

METHODS

Synthesis of PbS. The two smaller sized PbS QD samples were synthesized by a previously reported method.[51] The quantum dots were grown at either 60 or 120 °C using a half-size reaction to conserve reagents. Reaction times were between 10 and 90 min. Optical absorbance spectra show no significant change during that interval, which is consistent with the "size focusing" mechanism reported. The largest size PbS sample was prepared by a modification to the method of Hines.[52] First, 90 mg of PbO (Aldrich, >99%), 4 mL of oleic acid (Aldrich, 90%), and 4 mL of 1-octadecene (Aldrich, 90%) were heated under vacuum at 150 °C for 30 min, then brought to 100 °C under argon atmosphere. A solution of 42 μL of trimethylsilylsulfide (Aldrich) in 2 mL of 1-octadecene was quickly injected. Reaction products were removed after 1 min and cleaned by precipitation with dry and degassed acetone (2:1 with reaction solution) and centrifugation (8000 rpm for 8 min). The supernatant was discarded, and the samples were dispersed in carbon tetrachloride for optical characterization.

Synthesis of PbSe. All PbSe nanocrystals except the small reference sample discussed in the Supporting Information S8 were synthesized by slightly modifying a previously reported procedure.[7] All manipulations were carried out in a dry and oxygen-free environment. Specific amounts and times for individual particle sizes are reported in Table 2.

Lead(II) oxide (Aldrich, 99.999%) was mixed with oleic acid (Aldrich, 90%) and 1-octadecene (ODE) (Aldrich, 90%) in a three-necked flask with temperature couple control finger, reflux condenser, and septum to be heated under vacuum to 100 °C for at least 90 min on which a colorless solution was obtained. Meanwhile, a solution of 1.185 g of selenium powder (Aldrich, 99.99%) was dissolved in 15.0 mL of trioctylphosphine (TOP) (Strem Chemicals, >97%) on stirring for 2 h to obtain a 1.0 M solution of TOP-Se in TOP. Except for the largest particles used in this work, 130 μL of diphenylphosphine (DPP) (Aldrich, 98%) was added to the solution.

The solution containing the lead precursor was set to argon atmosphere and heated to 180 °C. The TOP-Se solution was rapidly injected on which the solution temperature dropped to 155−160 °C, and the heater was switched off. After the desired reaction time had passed, 10 mL of cold hexanes was carefully injected and it was additionally cooled with an external water bath.

The nanocrystals were precipitated by the addition of anhydrous ethanol, the suspension centrifuged for 5 min at 4500 rpm, the supernatant discarded, and the precipitate dissolved in anhydrous toluene. It was washed two more times on adding anhydrous methanol and one more time with acetone. Finally, the nanocrystals were stored in a 9:1 mixture of anhydrous hexanes/octane.

The PbSe nanocrystals shown in Supporting Information S8 were synthesized following Ma et al.[10]

Characterization. For vis−IR spectra, the nanocrystals were precipitated with ethanol and dissolved in anhydrous tetrachloroethylene. NIR cuvettes with the spectral window to 3000 nm and a path length of 10 mm were used to record spectra in a Shimadzu UV−vis−IR 3600 spectrometer with 0.5 nm step width.

For TEM imaging, one drop of the hexanes/octane solution of PbS(e) nanocrystals was cast on a gold grid coated with a thin amorphous carbon film and allowed to dry. Images were acquired with a FEI Tecnai 20 instrument operating at an acceleration voltage of 200 kV.

Conflict of Interest: The authors declare no competing financial interest.

Supporting Information Available: Code examples, additional TEM images, image processing, bulk absorption coefficients, PbSe PSDs during matching and values for constants a, b, and c, PSD results for different THS values, influence of thresholding on the band gap *vs* size relationship, and data of small and medium sized PbSe. This material is available free of charge *via* the Internet at http://pubs.acs.org.

REFERENCES AND NOTES

1. Patra, M. K.; Manoth, M.; Singh, V. K.; Gowd, G. S.; Choudhry, V. S.; Vadera, S. R.; Kumar, N. Synthesis of Stable Dispersion of ZnO Quantum Dots in Aqueous Medium Showing Visible Emission from Bluish Green to Yellow. *J. Lumin.* **2009**, *129*, 320–324.
2. Shalom, M.; Rühle, S.; Yahav, S.; Zaban, A. Energy Level Alignment in CdS Quantum Dot Sensitized Solar Cells Using Molecular Dipoles. *J. Am. Chem. Soc.* **2009**, *131*, 9876–9877.
3. Zhao, N.; Osedach, T. P.; Chang, L.-Y.; Geyer, S. M.; Wanger, D.; Binda, M. T.; Arango, A. C.; Bawendi, M. G.; Bulovic, V. Colloidal PbS Quantum Dot Solar Cells with High Fill Factor. *ACS Nano* **2010**, *4*, 3743–3752.
4. Hillhouse, H.; Beard, M. C. Solar Cells from Colloidal Nanocrystals: Fundamentals, Materials, Devices, and Economics. *Curr. Opin. Colloid Interface Sci.* **2009**, *14*, 245–259.
5. Bisquert, J. Physical Electrochemistry of Nanostructured Devices. *Phys. Chem. Chem. Phys.* **2008**, *10*, 49–72.
6. Konstantatos, G.; Sargent, E. H. Nanostructured Materials for Photon Detection. *Nat. Nanotechnol.* **2010**, *5*, 391–400.
7. Liu, Y.; Gibbs, M.; Puthussery, J.; Gaik, S.; Ihly, R.; Hillhouse, H. W.; Law, M. Dependence of Carrier Mobility on Nanocrystal Size and Ligand Length in PbSe Nanocrystal Solids. *Nano Lett.* **2010**, *10*, 1960–1969.
8. Tang, J.; Sargent, E. H. Infrared Colloidal Quantum Dots for Photovoltaics: Fundamentals and Recent Progress. *Adv. Mater.* **2011**, *23*, 12–29.
9. Kang, M. S.; Sahu, A.; Norris, D. J.; Frisbie, C. D. Size-Dependent Electrical Transport in CdSe Nanocrystal Thin Films. *Nano Lett.* **2010**, *10*, 3727–3732.
10. Ma, W.; Swisher, S. L.; Ewers, T.; Engel, J.; Ferry, V. E.; Atwater, H. A.; Alivisatos, A. P. Photovoltaic Performance of Ultrasmall PbSe Quantum Dots. *ACS Nano* **2011**, *5*, 8140–8147.
11. Chandler, R. E.; Houtepen, A. J.; Nelson, J.; Vanmaekelbergh, D. Electron Transport in Quantum Dot Solids: Monte Carlo Simulations of the Effects of Shell Filling, Coulomb Repulsions, and Site Disorder. *Phys. Rev. B* **2007**, *75*, 085325.
12. Zhitomirsky, D.; Kramer, I. J.; Labelle, A. J.; Fischer, A.; Debnath, R.; Pan, J.; Bakr, O. M.; Sargent, E. H. Colloidal Quantum Dot Photovoltaics: The Effect of Polydispersity. *Nano Lett.* **2012**, *12*, 1007–1012.
13. Viswanatha, R.; Sapra, S.; Satpati, B.; Satyam, P. V.; Dev, B. N.; Sarma, D. D. Understanding the Quantum Size Effects in ZnO Nanocrystals. *J. Mater. Chem.* **2004**, *14*, 661–668.
14. O'Reilly, E. P.; Lindsay, A.; Tomic, S.; Kamal-Saadi, M. Tight-Binding and KP Models for the Electronic Structure of Ga(In)NAs and Related Alloys. *Semicond. Sci. Technol.* **2002**, *17*, 870–879.
15. Riha, S. C.; Parkinson, B. A.; Prieto, A. L. Solution Based Synthesis and Characterization of Cu_2ZnSnS_4 Nanocrystals. *J. Am. Chem. Soc.* **2009**, *131*, 12054–12055.
16. Meulenkamp, E. A. Synthesis and Growth of ZnO Nanoparticles. *J. Phys. Chem. B* **1998**, *102*, 5566–5572.
17. Oskam, G.; Hu, Z.; Penn, R. L.; Pesika, N.; Searson, P. C. Coarsening of Metal Oxide Nanoparticles. *Phys. Rev. E* **2002**, *66*, 11403/1–11403/4.
18. Mićić, O. I.; Curtis, C. J.; Jones, K. M.; Sprague, J. R.; Nozik, A. J. Synthesis and Characterization of InP Quantum Dots. *J. Phys. Chem.* **1994**, *98*, 4966–4969.
19. Segets, D.; Gradl, J.; Klupp Taylor, R.; Vassilev, V.; Peukert, W. Analysis of Optical Absorbance Spectra for the Determination of ZnO Nanoparticle Size Distribution, Solubility and Surface Energy. *ACS Nano* **2009**, *3*, 1703–1710.
20. Pesika, N. S.; Stebe, K. J.; Searson, P. C. Relationship between Absorbance Spectra and Particle Size Distributions for Quantum-Sized Nanocrystals. *J. Phys. Chem. B* **2003**, *107*, 10412–10415.
21. Viswanatha, R.; Sarma, D. D. Study of the Growth of Capped ZnO Nanocrystals: A Route to Rational Synthesis. *Chem.—Eur. J.* **2006**, *12*, 180–186.
22. Marczak, R.; Segets, D.; Voigt, M.; Peukert, W. Optimum between Purification and Colloidal Stability of ZnO Nanoparticles. *Adv. Powder Technol.* **2010**, *21*, 41–49.
23. Segets, D.; Marczak, R.; Schäfer, S.; Paula, C.; Gnichwitz, J.-F.; Hirsch, A.; Peukert, W. Experimental and Theoretical Studies of the Colloidal Stability of Nanoparticles—A General Interpretation Based on Stability Maps. *ACS Nano* **2011**, *5*, 4658–4669.
24. Segets, D.; Hartig, M. A. J.; Gradl, J.; Peukert, W. A Population Balance Model of Quantum Dot Formation: Oriented Growth and Ripening of ZnO. *Chem. Eng. Sci.* **2012**, *70*, 4–13.
25. Kanazawa, H.; Adachi, S. Spectroellipsometry and Electroreflectance of PbS. *J. Appl. Phys.* **1998**, *84*, 5342–5344.
26. Suzuki, N.; Sawai, K.; Adachi, S. Optical Properties of PbSe. *J. Appl. Phys.* **1995**, *77*, 1249–1255.

27. Hens, Z.; Moreels, I. Light Absorption by Colloidal Semiconductor Quantum Dots. *J. Mater. Chem.* **2012**, *22*, 10406–10415.

28. Kang, I.; Wise, F. W. Electronic Structure and Optical Properties of PbS and PbSe Quantum Dots. *J. Opt. Soc. Am. B* **1997**, *14*, 1632–1646.

29. Rasband, W. S. *ImageJ*; National Institutes of Health, Bethesda, MD, 1997−2011; http://imagej.nih.gov/ij/.

30. Ridler, T. W.; Calvard, S. Picture Thresholding Using an Iterative Selection Method. *IEEE Trans. Syst. Man Cybern.* **1978**, *SMC-8*, 630–632.

31. Huang, L. K.; Wang, M.-J. J. Image Thresholding by Minimizing the Measures of Fuzziness. *Pattern Recognit.* **1995**, *28*, 41–51.

32. Otsu, O. A Threshold Selection Method from Gray-Level Histograms. *IEEE Trans. Syst. Man Cybern.* **1979**, *SMC-9*, 62–66.

33. Leschonski, K.; Alex, W.; Koglin, B. Teilchengrößenanalyse. *Chem.-Ing.-Tech.* **1974**, *46*, 23–26.

34. Lechner, M. D.; Cölfen, H.; Mittal, V.; Völkel, A.; Wohlleben, W. Sedimentation Measurements with the Analytical Ultracentrifuge with Absorption Optica: Influence of Mie Scattering and Absorption of the Particles. *Colloid Polym. Sci.* **2011**, *289*, 1145–1155.

35. Planken, K. L.; Cölfen, H. Analytical Ultracentrifugation of Colloids. *Nanoscale* **2010**, *2*, 1849–1869.

36. Moreels, I.; Lambert, K.; Smeets, D.; de Muynck, D.; Nollet, T.; Martins, J. C.; Vanhaecke, F.; Vantomme, A.; Delerue, C.; Allan, G.; *et al.* Size-Dependent Optical Properties of Colloidal PbS Quantum Dots. *ACS Nano* **2009**, *3*, 3023–3030.

37. Cademartiri, L.; Montanari, E.; Calestani, G.; Migliori, A.; Guagliardi, A.; Ozin, G. A. Size-Dependent Extinction Coefficient of PbS Quantum Dots. *J. Am. Chem. Soc.* **2006**, *128*, 10337–10346.

38. Borrelli, N. F.; Smith, D. W. Quantum Confinement of PbS Microcrystals in Glass. *J. Non.-Cryst. Solids* **1994**, *180*, 25–31.

39. Kane, R. S.; Cohen, R. E.; Silbey, R. Theoretical Study of the Electronic Structure of PbS Nanoclusters. *J. Phys. Chem.* **1996**, *100*, 7928–7932.

40. Moreels, I.; Lambert, K.; De Muynck, D.; Vanhaecke, F.; Poelman, D.; Martins, J. C.; Allan, G.; Hens, Z. Composition and Size-Dependent Extinction Coefficient of Colloidal PbSe Quantum Dots. *Chem. Mater.* **2007**, *19*, 6101–6106.

41. Dai, Q.; Wang, Y.; Li, X.; Zhang, Y.; Pellegrino, D. J.; Zhao, M.; Zou, B.; Seo, J. T.; Wang, Y.; Yu, W. W. Size-Dependent Composition and Molar Extinction Coefficient of PbSe Semiconductor Nanocrystals. *ACS Nano* **2009**, *3*, 1518–1524.

42. Lipovskii, A.; Kolobkova, E.; Petrikov, V.; Kang, I.; Olkhovets, A.; Krauss, T.; Thomas, M.; Silcox, J.; Wise, F.; Shen, Q.; *et al.* Synthesis and Characterization of PbSe Quantum Dots in Phosphate Glass. *Appl. Phys. Lett.* **1997**, *71*, 3406–3408.

43. Pietryga, J. M.; Schaller, R. D.; Werder, D.; Stewart, M. H.; Klimov, V. I.; Hollingsworth, J. A. Pushing the Band Gap Envelope: Mid-Infrared Emitting Colloidal PbSe Quantum Dots. *J. Am. Chem. Soc.* **2004**, *126*, 11752–11753.

44. Sashchiuk, A.; Langof, L.; Chaim, R.; Lifshitz, E. Synthesis and Characterization of PbSe and PbSe/PbS Core−Shell Colloidal Nanocrystals. *J. Cryst. Growth* **2001**, *240*, 431–438.

45. Steckel, J. S.; Coe-Sullivan, S.; Bulovic, V.; Bawendi, M. G. 1.3 μM to 1.55 μM Tunable Electroluminescence from PbSe Quantum Dots Embedded within an Organic Device. *Adv. Mater.* **2003**, *15*, 1862–1866.

46. Koole, R.; Allan, G.; Delerue, C.; Meijerink, A.; Vanmaekelbergh, D.; Houtepen, A. J. Optical Investigation of Quantum Confinement in PbSe Nanocrystals at Different Points in the Brillouin Zone. *Small* **2008**, *4*, 127–133.

47. Lu, W.; Fang, J.; Ding, Y.; Wang, Z.-L. Formation of PbSe Nanocrystals: A Growth towards Nanocubes. *J. Phys. Chem. B* **2005**, *109*, 19219–19222.

48. Houtepen, A. J.; Koole, R.; Vanmaekelbergh, D.; Meeldijk, J.; Hickey, S. G. The Hidden Role of Acetate in the PbSe Nanocrystal Synthesis. *J. Am. Chem. Soc.* **2006**, *128*, 6792–6793.

49. Cho, K.-S.; Talapin, D. V.; Gaschler, W.; Murray, C. B. Designing PbSe Nanowires and Nanorings through Oriented Attachment of Nanoparticles. *J. Am. Chem. Soc.* **2005**, *127*, 7140–7147.

50. Allan, G.; Delerue, C. Confinement Effects in PbSe Quantum Wells and Nanocrystals. *Phys. Rev. B* **2004**, *70*, 245321.

51. Fu, H.; Tsang, S.-W.; Zhang, Y.; Ouyang, J.; Lu, J.; Yu, K.; Tao, Y. Impact of the Growth Conditions of Colloidal PbS Nanocrystals on Photovoltaic Device Performance. *Chem. Mater.* **2011**, *23*, 1805–1810.

52. Hines, M. A.; Scholes, G. D. Colloidal PbS Nanocrystals with Size-Tunable Near-Infrared Emission: Observation of Post-Synthesis Self-Narrowing of the Particle Size Distribution. *Adv. Mater.* **2003**, *15*, 1844–1849.